Applied Catalysis B: Environmental 186 (2016) 30–40

Contents lists available at ScienceDirect

Applied Catalysis B: Environmental

journal homepage: www.elsevier.com/locate/apcatb

Catalytic oxidation and adsorption of Hg^0 over low-temperature NH_3-SCR $LaMnO_3$ perovskite oxide from flue gas

Haomiao Xu, Zan Qu, Chenxi Zong, Fuquan Quan, Jian Mei, Naiqiang Yan*

School of Environmental Science and Engineering, Shanghai Jiao Tong University, Shanghai 200240, China

ARTICLE INFO

Article history:
Received 9 July 2015
Received in revised form
23 December 2015
Accepted 24 December 2015
Available online 29 December 2015

Keywords:
Perovskite
Elemental mercury (Hg^0)
Manganese oxides
Catalytic oxidation

ABSTRACT

To simultaneously remove elemental mercury (Hg^0) and NO_x at low temperature from flue gas in coal-fired power plants, an efficient NH_3-SCR $LaMnO_3$ perovskite oxide was chosen as the catalyst for Hg^0 removal. The physicochemical properties, surface reaction and mercury desorption were investigated using BET, XRD, XPS, H_2-TPR and Hg-TPD, to investigate the Hg^0 capture mechanism over $LaMnO_3$ oxides. The results indicated that $LaMnO_3$ exhibits a Hg^0 capacity that is as high as 6.22 mg/g (600 min) at 150 °C. O_2 enhanced the Hg^0 removal performance by re-oxidation of reduced Mn^{3+} to Mn^{4+} and providing additional adsorbed oxygen. NO enhanced the Hg^0 removal performance. However, NH_3 exhibited negative effects on Hg^0 removal. The $NH_3 + O_2$-TPD and $NO + O_2$-TPD results indicated that the ad-NH_3 species prevent Hg^0 adsorption, but the ad-NO_2 species were beneficial for Hg^0 oxidation. The effects of SO_2 and H_2O were also investigated, and the results indicated that they inhibited Hg^0 removal. Hg-TPD under different reaction atmospheres was employed to further investigate the combing state of Hg^0 on $LaMnO_3$ surface, the results indicated that mercury primarily existed as Hg–O, and $LaMnO_3$ can be regenerated using thermal desorption.

1. Introduction

Elemental mercury (Hg^0) in the atmosphere is hazardous for human and the environment [1–3]. The Minamata Convention on Mercury signed aiming at controlling mercury emission globally. Among the various emission sources, coal-fired power plants are major anthropogenic mercury emission sources [4,5]. In China, approximately 38% of the Hg^0 is emitted from coal-fired flue gas [5]. Currently, Hg^0 removal technologies are often part of the available equipment for co-beneficial mercury control (e.g., using SCR catalysts for the oxidation of Hg^0 to oxidized mercury (Hg^{2+}), followed by Hg^{2+} removal in wet flue gas desulfurization (WFGD) system) [6–8]. Another method was adsorption technology, and activated carbon injection (ACI) technology makes full use of AC to adsorb Hg^0. In addition, the particle-bound mercury (Hg^p) is removed along with fly ash in the ESP/FF system [9,10]. However, the Hg^{2+} enriched in the WFGD system or mercury in the fly ashes could cause secondary mercury contamination [7,11]. Furthermore, the use of the ACI technology was limited due to its high cost, dependences on the type of coal, inlet mercury concentration and reaction temperature [12,13].

In addition, more strict regulation aims to approach zero emission in coal-fired power plants, and the emission concentration should be $NO_x \leq 5\ mg/m^3$ and $Hg^0 \leq 0.002\ mg/m^3$. However, in many coal-fired power plants, the space required for the installation of deNO_x unit that operate at flue gas temperature of 350–400 °C is insufficient. To avoid deactivation of SCR catalyst and reduce costs, the proposed additional deNO_x technologies could be loaded downstream of the particle control devices where the flue gas temperature is lower than 200 °C. However, traditional SCR catalysts (V-W-TiO_2/V-Mo-TiO_2) may lose their activity at this low temperature. Moreover, without SCR catalysts in the coal-fired power plants, Hg^0 is difficult oxidized to Hg^{2+} [14,15]. Therefore, to simultaneously remove NO_x and Hg^0, the low-temperature deNO_x technology along with Hg^0 capture needs to be improved.

In previous studies, low-temperature NH_3-SCR technology had been widely studied and appears to be a potential method for NO removal. Many transition metal oxides such as MnO_x, FeO_x, V_2O_5, and CoO_x have been employed as catalysts for NO removal [16–19]. Mn-based oxides attracted much attention for capturing Hg^0 due to their high redox potential, low cost and environmental friendliness [20]. The valance state of Mn and the existing state of O are important for the removal of Hg^0. During the Hg^0 removal process,

* Corresponding author. Fax: +86 21 54745591.
E-mail address: nqyan@sjtu.edu.cn (N. Yan).

http://dx.doi.org/10.1016/j.apcatb.2015.12.042
0926-3373/

Hg^0 oxidized to Hg^{2+} on the surface of MnO_x, followed by reduction of high valance Mn^{4+} to Mn^{3+} or Mn^{2+}. Then the oxidized mercury exists as Hg–O on the surface of the Mn-based materials. Among various Mn-based low-temperature NH_3-SCR catalysts, perovskite type Mn-based oxides have recently attracted growing interest as alternative catalysts due to their low cost, high catalytic activity and strong thermal stability [21–25]. The general chemical formula for perovskite oxide is ABO_3, in which the A ions can be rare earth and alkaline ions, and the B ions are often first-row transition metal ions. The catalytic properties are primarily due to the abnormal valence of the B ion, which is induced by the electric neutrality principle. The Mn ions can occupy the B site of perovskite oxides. The abundance of adsorbed oxygen and the oxygen valance may result in Hg^0 oxidation. $LaMnO_3$ exhibited a higher catalytic oxidation performance than that of other Mn-based perovskite oxides. In addition, $LaMnO_3$ had been used as low-temperature catalyst for NO removal. However, there was still no attempt for the catalytic oxidation of Hg^0 using NH_3-SCR catalysts.

Herein, $LaMnO_3$ perovskite oxides were synthesized for the removal of Hg^0. A fixed-bed reaction system was constructed to investigate the Hg^0 removal performance. The effects of O_2, NH_3, NO, H_2O and SO_2 flue gas components were considered in our study and the mechanism for Hg^0 capture under different gas components is discussed. Furthermore, the mercury desorption performance was also investigated in our study.

2. Experimental

2.1. Catalyst preparation

The $LaMnO_3$ catalysts were prepared using a sol–gel method. Briefly, the required amount of La(NO3) 3 and Mn(NO3) 3 was dissolved in diluted water, followed by the addition of citric acid (CA) to the mixture. The temperature of the aqueous solution was maintained at 80 °C. The molar ratio of La:Mn:CA was 1:1:2. After vigorous stirring and evaporation, a transparent gel was formed, which was dried at 100 °C overnight. The obtained precursor was calcined at 300 °C for 1 h in air to completely decompose citric acid followed by calcination at 750 °C for 5 h at a rate of 10 °C/min. For comparison, MnO_x and LaO_x were also synthesized according to the same sol–gel method.

2.2. Physical characterization

The materials were characterized and analyzed using various techniques. The crystallinity of the fresh samples were determined by X-ray diffraction (XRD, APLX-DUO, BRUKER, Germany) on with Cu-Kα radiation. The XRD patterns were recorded in a 2θ range from 10° to 80° at a scanning rate of 5 °/min. The multipoint Brunauer–Emmett–Teller (BET) surface was analyzed using a N_2 sorption measurement (Nova-2200 e) at 77 K. The pore diameter and pore volume were calculated based on the Barrett–Joyner–Halenda (BJH) method. X-ray photoelectron spectroscopy (XPS, Shimadzu–Kratos) was used to examine the valance states of the elements on the surface of the materials. This instrument coupled with an ultra DLD spectrometer with an Al Kα excitation source. The C 1s line at 284.6 eV was employed as a reference for the binding energy calibration. The morphology and structure of as-prepared materials were observed via a transmission electron microscopy (TEM), and the images were using a JEOLJEM-2010 TEM electron microscope operating at 200 kV. The reducibility of the samples was determined using H_2-TPR experiments, and these experiments were performed on a Chemisorp TPx 290 instrument. The samples were degassed at 200 °C for 3 h under an Ar atmosphere prior to the tests, and the reducing gas consisted of 10% H_2/Ar.

$NH_3 + O_2$ and $NO + O_2$-temperature programmed desorption ($NH_3 + O_2$-TPD and $NO + O_2$-TPD) was performed using the fixed-bed adsorption system shown in Fig. 1. A FT–IR gas analyzer was employed to detect the gas components along with the increase in temperature. 20 mg of each sample was pre-treated by 500 ppm NH_3 + 4% O_2 (for $NH_3 + O_2$-TPD) and 500 ppm NO + 4% O_2 (for $NO + O_2$-TPD) at 50 °C, until the NH_3 or NO concentration did no change. $NH_3 + O_2$ and $NO + O_2$ were balanced with pure N_2 (total flow rate = 500 ml/min). Then, the fixed-bed temperature was increased at a rate of 10 °C/min and NO, NH_3, N_2O and NO_2 were detected and recorded using a FT–IR gas analyzer.

2.3. Hg^0 removal tests

The Hg^0 removal activities were evaluated using a fixed-bed reactor, and a schematic representation of the Hg^0 adsorption system is shown in Fig. 1. An Hg^0 permeation tube was used to generate Hg^0 vapor carried by pure N_2, which was introduced to the inlet of the gas mixer. Other gases including NO, O_2, SO_2, and H_2O vapor were introduced to the gas mixer at constant flow rates. NH_3 was separately introduced into the simulated flue gas. The flow rate was controlled by mass flow controllers (MFC) and the total flow rate was set to 200–500 ml/min. A fixed-bed reactor system was used to investigate the Hg^0 adsorption performance. The reaction temperature was controlled from 50 to 350 °C by a temperature controller tubular furnace. A cold vapor atomic absorption spectroscopy (CVASS) analyzer was employed as an online continuous detector that could only detect Hg^0. The concentration of Hg^0 was measured using Lumex RA 915+. The inlet concentration of Hg^0 was 100–500 μg/m^3. At the beginning of each test, the simulated gas bypassed the reactor and the inlet gas was detected to ensure a stable Hg^0 concentration. Then the simulated gas passed the samples and the Hg^0 concentration was detected by CVASS online system.

The Hg^0 removal efficiency and adsorption capacities were calculated according to Eqs. (1) and (2):

$$\eta = \frac{Hg^0_{in} - Hg^0_{out}}{Hg^0_{in}} \quad (1)$$

$$Q = \frac{1}{m}\int_{t_2}^{t_1} \left(\frac{Hg^0_{in} - Hg^0_{out}}{Hg^0_{in}}\right) \times f \times dt \quad (2)$$

$$\text{NO removal efficiency} = \frac{NO_{in} - NO_{out}}{NO_{in}} \quad (3)$$

where η is the Hg^0 removal efficiency, $Hg_{in}{}^0$ is the inlet concentration of Hg^0, $Hg_{out}{}^0$ is the outlet concentration of Hg^0, Q is the Hg^0 adsorption capacity, m is the mass of the sorbent in the fixed-bed, f is the flow rate of the influent, and t_0 and t_1 are the initial and final test times, respectively, of the breakthrough curves.

2.4. NH_3-SCR catalytic activity measurement

The NH_3-SCR experiments were also performed in a fixed bed system. The experiments were performed according to the procedures employed in the Hg^0 adsorption tests. 20 mg sample was inserted into the reactor under an atmosphere consisting of 500 ppm NH_3, 500 ppm NO and 4% O_2, which was balanced by N_2, at a total flow rate of 500 ml/min. The temperature ranged from 100 to 300 °C. The FT–IR gas analyzer was employed to detect the gas component in the outlet of the flue gas.

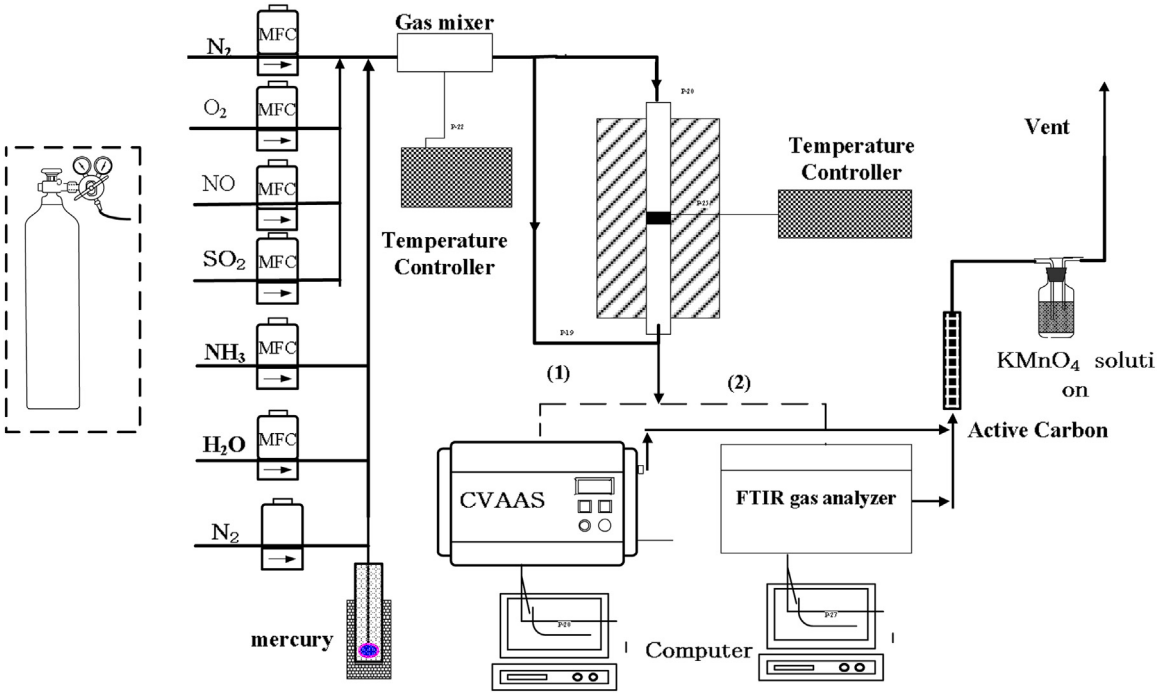

Fig. 1. Flow process of Hg^0 adsorption and the NH_3-SCR assessment system.

2.5. Regeneration measurement

The mercury temperature programmed desorption (Hg-TPD) method was developed to evaluate the desorption performance of $LaMnO_3$. Prior to each test, the sorbents were adsorbed for 20 min at 150 °C with N_2 (for N_2 + Hg-TPD), 4% O_2 (for O_2 + Hg-TPD), 4% O_2 + 500 ppm NH_3 (for O_2 + NH_3 + Hg-TPD), 4% O_2 + 500 ppm NO (for O_2 + NO + Hg-TPD) and 4% O_2 + 500 ppm SO_2 (for O_2 + SO_2 + Hg-TPD). After the furnace cooled to 100 °C, the sorbents were regenerated by heating from 100 to 700 °C in a pure N_2 carrier gas. The heating rates were set to 2, 5 and 10 °C/min. The mercury signal was recorded by a CVASS online system.

3. Results and discussion

3.1. Physicochemical properties

Fig. 2 shows the XRD patterns of the LaO_x, MnO_x and $LaMnO_3$ samples. For the LaO_x samples, the peaks were assigned to the $La(OH)_3$ diffraction pattern (JCPDS 83-2034) and La_2O_3 diffraction pattern (JCPDS 05-0602) [26]. For MnO_x, Mn_2O_3 (JCPDS 24-0508) was the primary phase, and only a few peaks were ascribed to other crystalline manganese oxides. However, for $LaMnO_3$, the peaks were located at 22.8, 32.6, 40.2, 46.7, 52.8, 58.1, 68.3 and 77.8°, and all of these characteristic peaks can be well indexed to a perovskite phase (PDF-88-0633) with a rhombohedral structure.

The N_2 adsorption–desorption isotherms and pore size distributions of $LaMnO_3$ were investigated, and the results are shown in Table 1. The BET surface area of the prepared $LaMnO_3$ was 16.6 m^2/g, and the total pore volume and average pore diameter were 0.118 cm^3/g and 11.5 nm, respectively. For comparison, the BET surface areas of La_2O_3 and MnO_x were also calculated. The BET surface area of La_2O_3 was 2.3 m^2/g, which was smaller than that of $LaMnO_3$, and the pore volume was 0.068 cm^3/g, which was also smaller than that of $LaMnO_3$. For MnO_x, the BET surface area was 11.2 m^2/g, and the pore volume and pore diameter were 0.051 cm^3/g and 3.308 nm, respectively. To further elucidate the textural properties of $LaMnO_3$, the TEM image is shown in Fig. S1, the uniform crystal lattice was indicative of the perovskite structure. In addition, the EDS analysis indicated that the elemental components were La, Mn and O.

Table 1
Textural properties (BET surface area, pore volume and pore diameter) of the as-prepared samples.

Materials	BET surface area (m^2/g)	Pore volume (cm^3/g)	Pore diameter (nm)
La_2O_3	2.3	0.068	3.34
MnO_x	11.2	0.051	3.30
$LaMnO_3$	16.6	0.118	11.5

Nest, the valance states of the elements were characterized by XPS. The results are reported in Fig. 3(a). For the Mn 2 p spectrum of $LaMnO_3$, the peaks at 643.7 and 641.7 eV were correspond to Mn^{4+} and Mn^{3+}, respectively [27]. The ratio of Mn^{4+}/Mn^{3+} was determined to be 33.93/66.07. A higher valence state of Mn may result in a higher catalytic oxidation activity [28,29]. The state of O was also evaluated by XPS analysis, as shown in Fig. 3B, in the O 1s spectrum of $LaMnO_3$, the peaks located at 531.0 and 529.6 eV were ascribed to the lattice oxygen (O_{latt}) and adsorbed oxygen (O_{ads}), respectively [30]. The ratio of O_{latt}/O_{ads} was approximately 47.51/52.49 in the fresh samples. The adsorbed oxygen was favorable for Hg^0 capture [29,31].

3.2. Hg^0 removal over NH_3-SCR $LaMnO_3$ perovskite oxide

3.2.1. NH_3-SCR performance over $LaMnO_3$

$LaMnO_3$ has been previously used as a low-temperature NH_3-SCR catalyst for NO removal from coal-fired flue gas [32]. As shown in Fig. 4(a), the NH_3-SCR performance of LaO_x, MnO_x and $LaMnO_3$ were tested. LaO_x exhibited almost no activity for NO removal. MnO_x exhibited a NO conversion of approximately 20% at 250 °C. However, for $LaMnO_3$, the NO conversion was higher than 65% at 200 °C. When the temperature increased from 250 to 350 °C, the NO conversion efficiency decreased. The Mn-based materials lost their activity for NO conversion at higher temperature (>200 °C). This

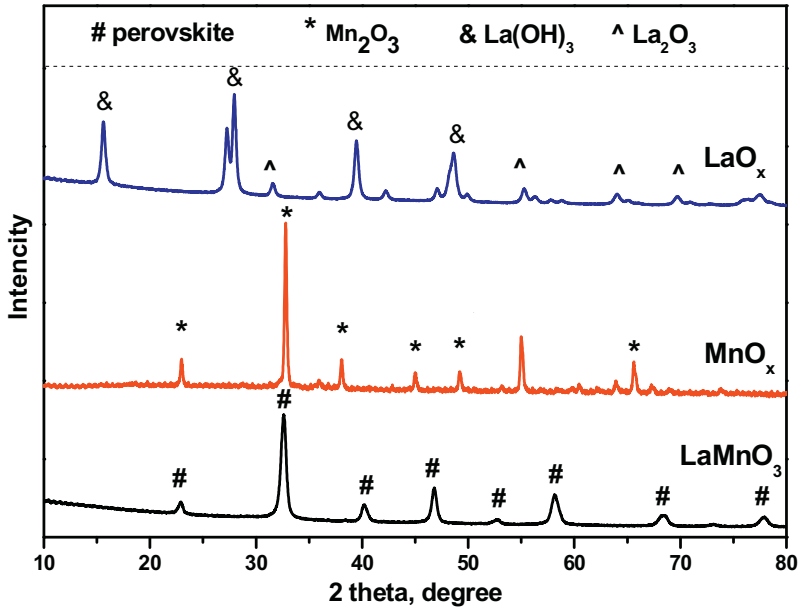

Fig. 2. XRD patterns of the LaO_x, MnO_x and $LaMnO_3$ samples.

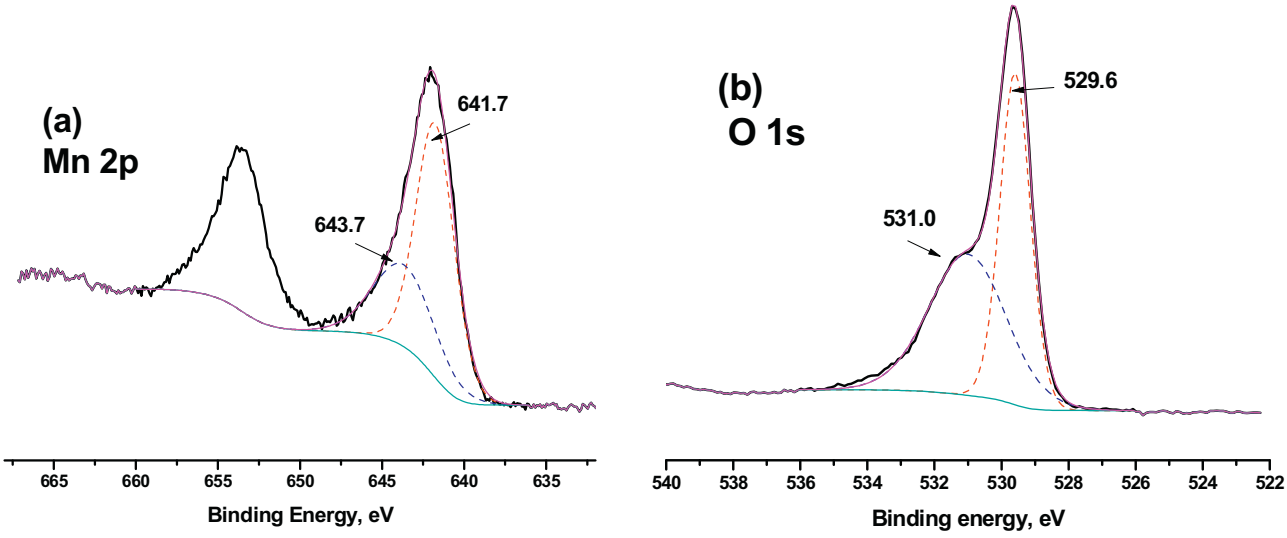

Fig. 3. XPS spectra of fresh $LaMnO_3$ over the spectral regions of (a) Mn 2 p and (b) O 1s.

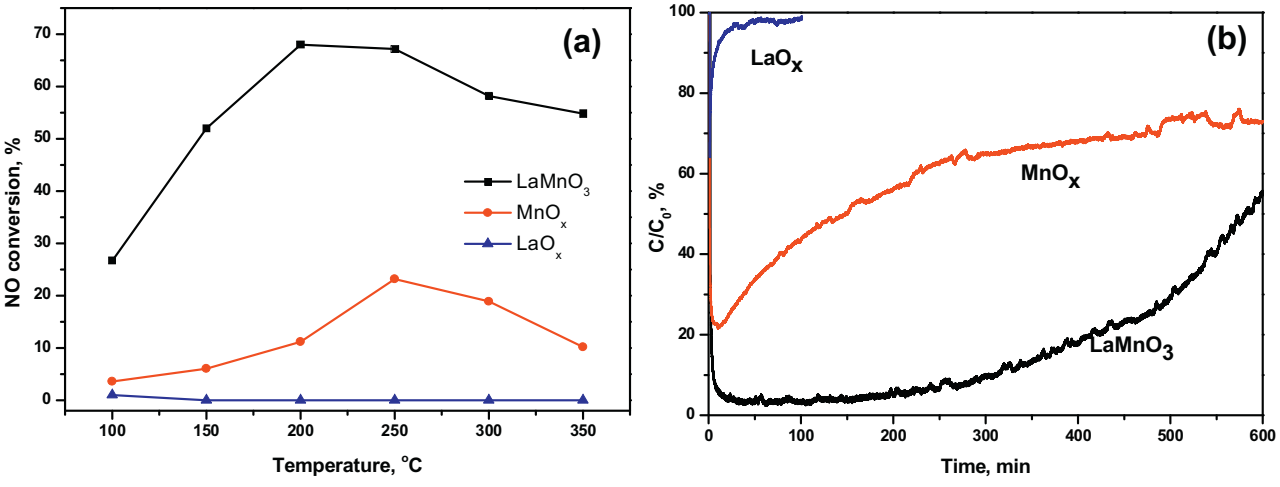

Fig. 4. Performance of (a) NO conversion and (b) Hg^0 removal over LaO_x, MnO_x and $LaMnO_3$; Reaction condition: GHSV = 478,000 h^{-1} and 4% O_2.

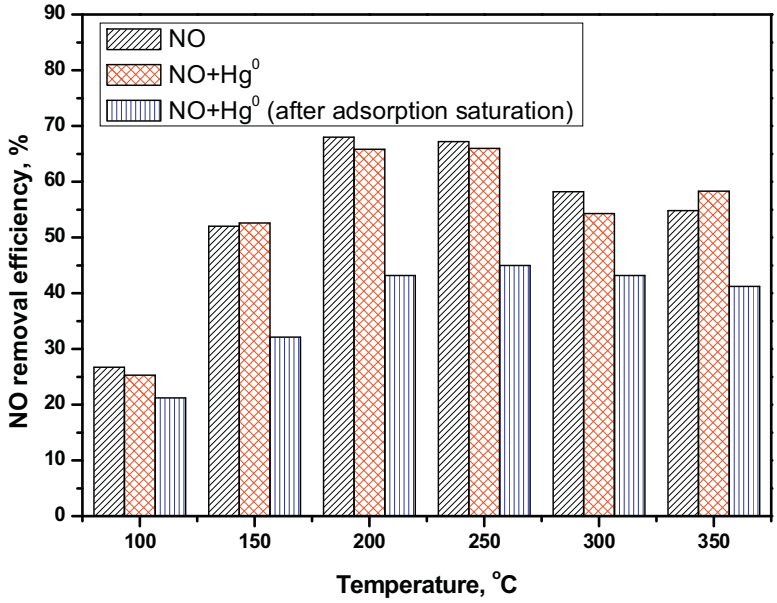

Fig. 5. The effect of Hg^0 on NO removal efficiency. (Reaction conditions: NO = NH_3 = 500 ppm, Hg^0 = 500 μg/m^3, O_2 = 4%, GHSV = 478,000 h^{-1} and N_2 as balance.).

temperature window (100–200 °C), it is beneficial for Hg^0 capture downstream from ESP or FF in the coal-fired power plants.

3.2.2. *Hg^0 adsorption activity over $LaMnO_3$*

To investigate the role of the perovskite crystal structure on Hg^0 removal, the adsorption test was performed in a fix-bed adsorption system. As shown in Fig. 4(b), Hg^0 removal activity increased in the following order: LaO_x « MnOx < $LaMnO_x$. LaO_x oxide exhibited almost no activity for Hg^0 removal. MnO_x gradually lost its Hg^0 removal ability, and the Hg^0 removal efficiency was only approximately 30% after 600 min reaction. $LaMnO_3$ achieved the best performance with a Hg^0 removal efficiency that was higher than 85% after 600 min reaction. The saturation adsorption capacity of $LaMnO_3$ for Hg^0 was calculated to be approximately 7.65 mg/g. The effect of Hg^0 on NO removal was also investigated. As shown in Fig. 5, in the presence of Hg^0, it existed a slight decrease for the removal of NO. But the trend was similar. It indicated that the addition of Hg^0 in the simulated gas had little effect on the NO removal. To further confirm the NO removal performance, the sample was first used for Hg^0 adsorption, and after adsorption saturation, the sample was used for NO removal. The NO removal efficiencies decreased sharply, especially at low temperature. Mn is most likely the main active site for Hg^0 removal based on previous reported results [29,31,33]. The high activity of $LaMnO_3$ was due to the benefit of perovskite crystal structure [34]. Mn^{n+} exhibited a better dispersion in the perovskite structure where it was located in the B sites of the lattice. The highly dispersed Mn^{n+} was beneficial for the Hg^0 catalytic oxidation on its surface [34]. Based on the characterization results, $LaMnO_3$ had the largest BET surface area, which was approximately 50% larger than that of MnO_x. The larger surface area was beneficial for physical adsorption. However, the large surface area was not the primary reason for the higher Hg^0 removal efficiencies. In our previous studies, the BET surface areas of Mn-based materials were larger than $LaMnO_3$ [35,36]. Therefore, the perovskite structure of $LaMnO_3$ contributed to the high catalytic activity for Hg^0 removal.

The effects of the Hg^0 initial concentration, gas hourly space velocity (GHSV) and temperature were investigated. As shown in Fig. 6(a), the initial Hg^0 concentrations were set to 100, 300 and 500 μg/m^3, respectively. When the initial Hg^0 concentration was 500 μg/m^3, the Hg^0 removal efficiency was approximately 50% after 600 min adsorption. However, when the initial Hg^0 concentration decreased to 300 μg/m^3, the Hg^0 removal efficiency was higher than that at an initial Hg^0 concentration of 500 μg/m^3 after 600 min adsorption. When the initial Hg^0 concentration was further decreased to 100 μg/m^3, the removal efficiency was maintained at a value higher than 95%. The effect of the GHSV was also investigated. The GHSV was set by changing the total gas flow rate. The GHSVs were 478,000, 286,800 and 95,600 h^{-1} when the total flow rates were 500, 300 and 100 ml/min, respectively. As shown in Fig. 6(b), the Hg^0 removal efficiency increased when the GHSV decreased. The Hg^0 removal efficiency (after 600 min adsorption) was approximately 90% when the GHSV decreased to 95,600 h^{-1}. To further investigate the Hg^0 removal mechanism over $LaMnO_3$ and the effects of the gas components, the reaction conditions were set to 500 μg/m^3 of inlet Hg^0 and GHSV = 478,000 h^{-1} even though the removal efficiency was not high under this condition. The effect of temperature was also investigated, and the temperature window ranged from 100 to 300 °C. The Hg^0 capacities increased from 6.13 mg/g at 100 °C to 6.22 mg/g at 150 °C. However, when the temperature increased from 150 to 300 °C, the Hg^0 capacity decreased to only 3.01 mg/g at 300 °C. The higher temperature resulted in $LaMnO_3$ losing its performance for Hg^0 removal. Manganese oxides may exhibit better activity at low temperature [35,37]. Herein, to gain insight into the $LaMnO_3$ sorbents, the reaction temperature were set to 150 °C, the inlet concentration was 500 μg/m^3 and the GHSV was 478,000 h^{-1}.

3.2.3. *Effect of O_2 on Hg^0 adsorption*

In general, the Hg^0 removal mechanism over Mn-based oxides involves the chemical adsorption. The catalytic oxidation of Hg^0 to Hg^{2+} enhanced the performance for Hg^0 capture. O_2 is the common oxidants of Hg^0 oxidation. Pure physical adsorption does not result in higher Hg^0 capacities. The adsorption experiments under pure N_2 were performed, and the results are shown in Fig. 7. $LaMnO_3$ exhibited a gradual decrease in its Hg^0 removal performance. After 125 min adsorption, the Hg^0 removal efficiency was only 50%. However, when 4% O_2 was added to the simulated gas, the Hg^0 removal efficiency increased. The existence of O_2 in the flue gas participated in the Hg^0 removal process. The Hg^0 removal experiments under pure N_2, 4% O_2 and 8% O_2 during a 600 min reaction were further investigated. The Hg^0 adsorption capacities were calculated and are

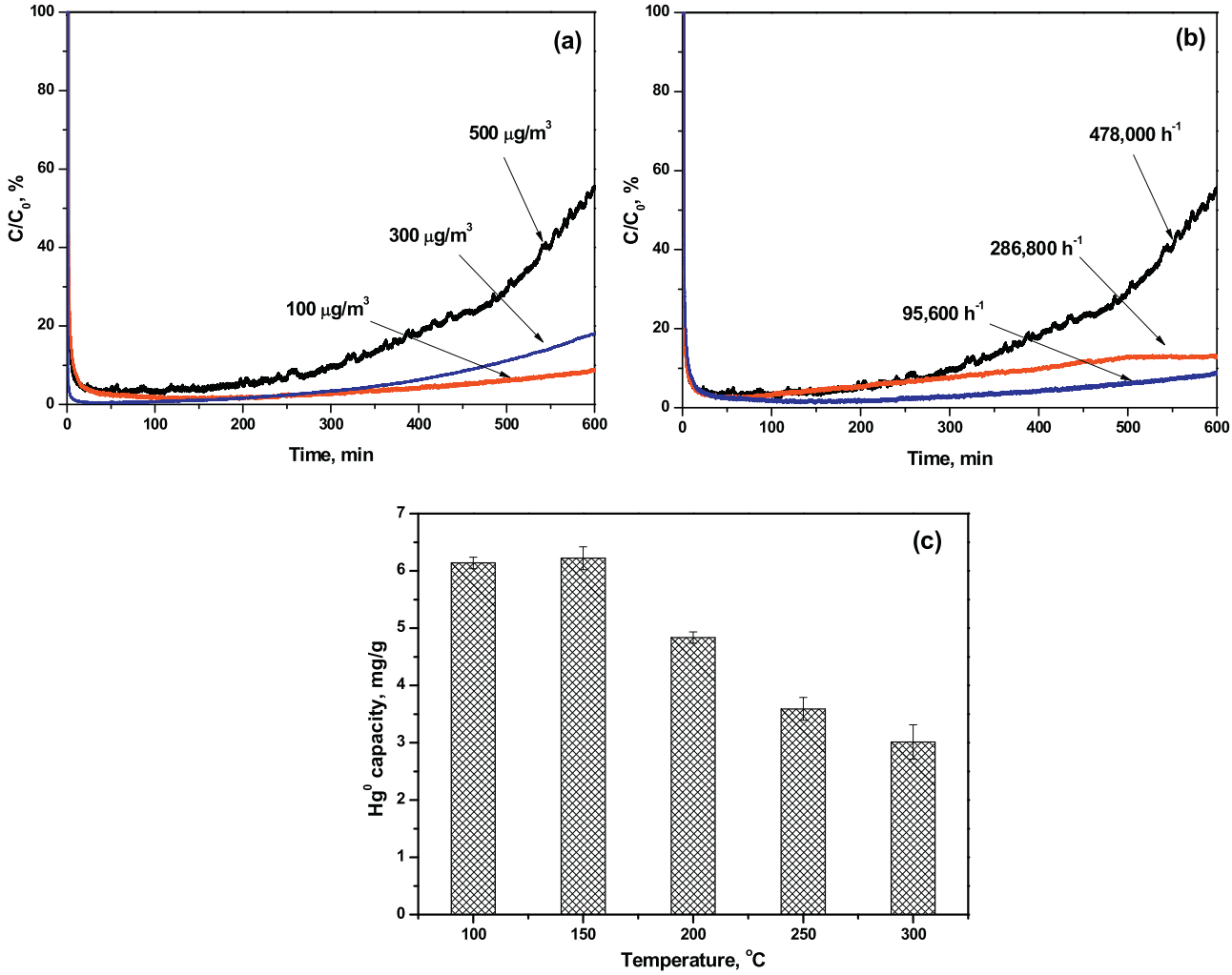

Fig. 6. (a) Effect of initial Hg^0 concentration, (b) gas hourly space velocity (GHSV), and (c) temperature on Hg^0 adsorption over $LaMnO_3$. Reaction condition: 4% O_2.

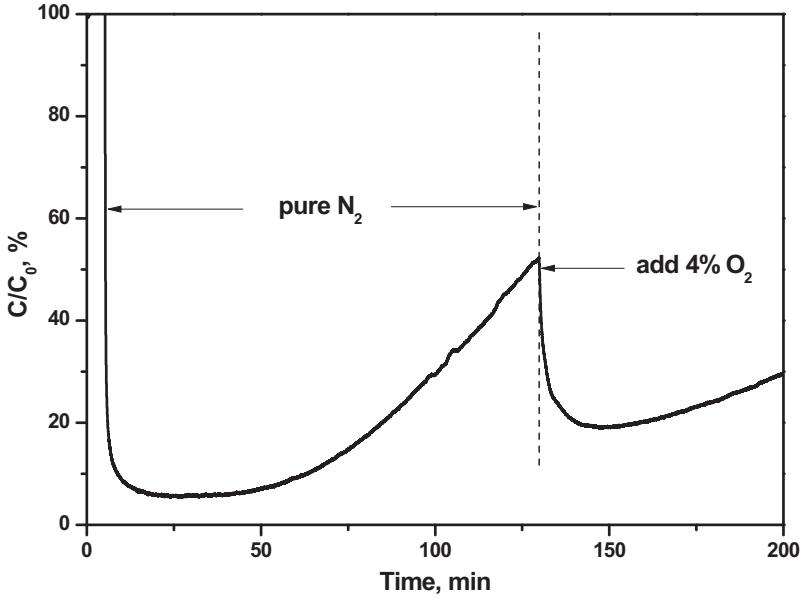

Fig. 7. Effect of O_2 on Hg^0 removal. Reaction condition:150 °C; GHSV = 478,000 h^{-1}; 4% O_2.

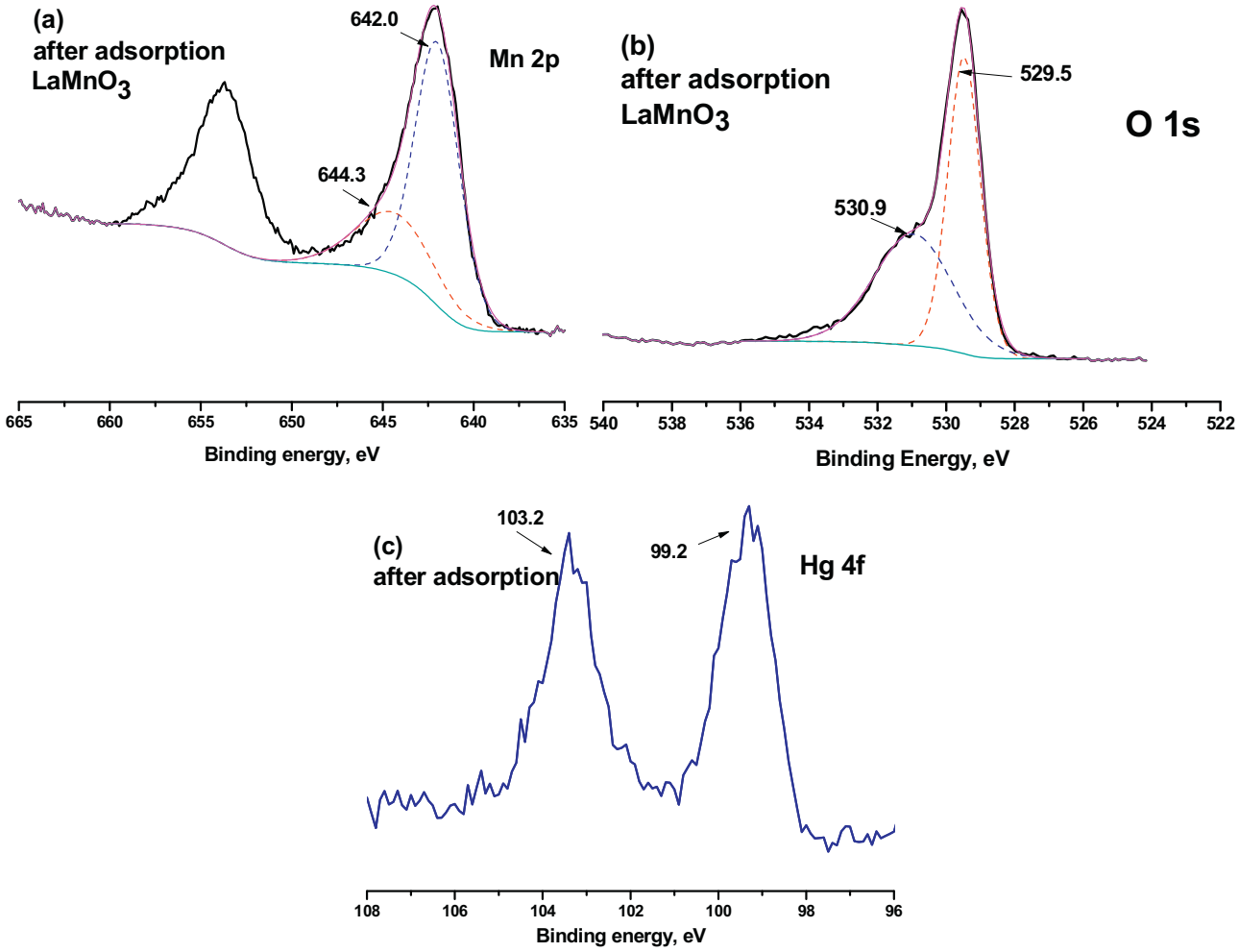

Fig. 8. XPS spectra of the $LaMnO_3$ sample after adsorption: (a) Mn 2p, (b) O 1s and (c) Hg 4f.

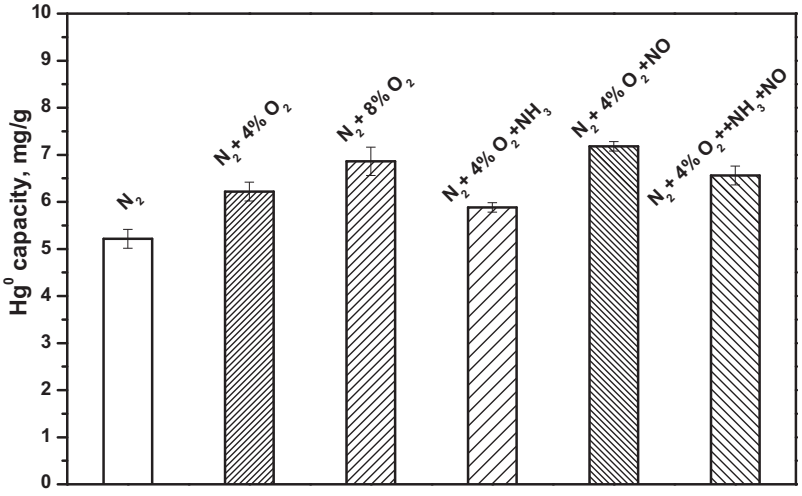

Fig. 9. Hg^0 capacities under pure N_2, 4% O_2, 8% O_2, 4%O_2 + 500 ppm NH_3, 4% O_2 + 500 ppm NO, and 4% O_2 + 500 ppm NO +500 ppm NH_3.Reaction condition: 150 °C and GHSV = 478000 h^{-1}.

shown in Fig. 9, the Hg^0 capacity decreased by approximately 17% in the absence of O_2. When the concentration of O_2 was increased to 8%, the Hg^0 capacities increased from 6.2 mg/g to approximately 6.8 mg/g. The H_2-TPR profile of $LaMnO_3$ is shown in Fig. S2. The peaks centered at 330.5 (peak 1) and 741.1 °C (peak 2) were due to the reduction of Mn^{4+} to Mn^{3+} and Mn^{3+} to Mn^{2+}, respectively. The peak 1/peak 2 ratio was 56.8/43.2. The results indicated the boundaries between Mn^{4+} to Mn^{3+} and Mn^{3+} to Mn^{2+}.

After adsorption, the XPS spectra of Mn 2p, O 1s and Hg 4f were recorded, and the results are shown in Fig. 8. In the XPS spec-

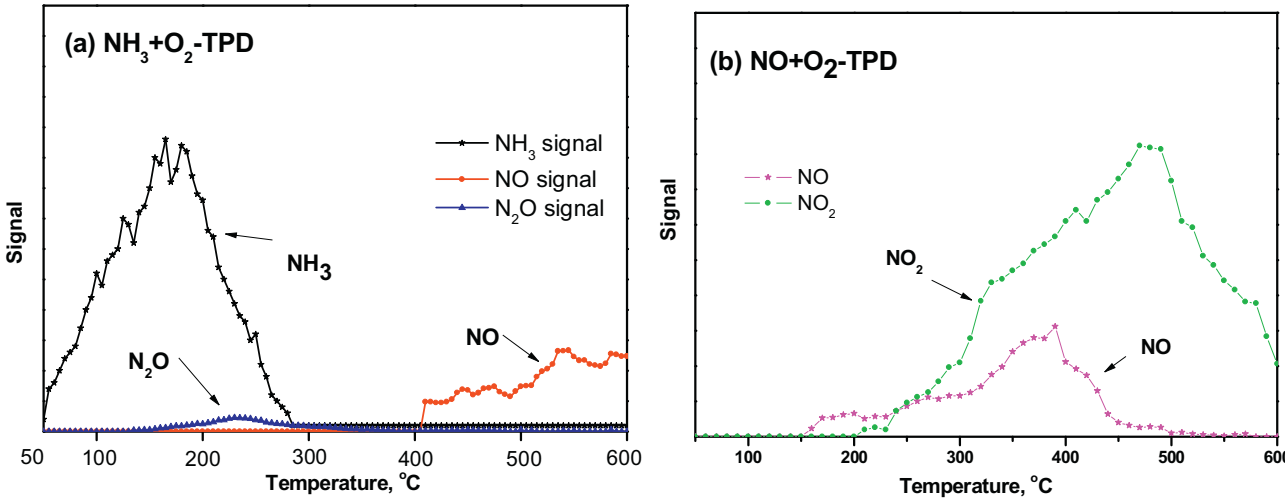

Fig. 10. (a) $NH_3 + O_2$-TPD, and (b) $NO + O_2$-TPD profiles over the $LaMnO_3$ samples.

tra of Mn 2p shown in Fig. 8(a), the Mn^{4+}/Mn^{3+} ratio changed to 29.14/70.86. A portion of the Mn^{4+} changed to Mn^{3+} during the adsorption process. After adsorption, (Fig. 8(b)), the O_{latt}/O_{ads} ratio was approximately 48.05/51.05, and the ratio decreased due to an increase in O_{ads} on the surface of $LaMnO_3$. The oxygen in the flue gas was first adsorbed on the surface of $LaMnO_3$ to generate O_{ads}. This O_{ads} combined with Hg^0 which was also adsorbed on the surface of $LaMnO_3$. To further confirm the results, the XPS spectrum of Hg 4f is shown in Fig. 8(c), and the peaks located at 103.2 and 99.2 eV were ascribed to HgO. The adsorbed Hg^0 existed as HgO on the surface of $LaMnO_3$. The mechanism of Hg^0 adsorption can be illustrated as follows:

$$Hg^0(g) \rightarrow Hg^0(ads) \quad (4)$$

$$Mn^{4+} \equiv O(ads) + Mn^{4+} \equiv O(ads) + Hg^0(ads) \rightarrow Mn^{3+} \equiv O - Hg(ads) + Mn^{3+} \equiv O(ads) \quad (5)$$

$$Mn^{3+} \equiv O(ads) + \frac{1}{2}O_2 \rightarrow Mn^{4+} \equiv O_2(ads) \quad (6)$$

3.2.4. Effect of NH_3 and NO on Hg^0 removal

$LaMnO_3$ was used as the low temperature NH_3-SCR catalyst in previous studies. As shown in Fig. 9, the effects of NH_3 and NO on the Hg^0 adsorption capacities was presented. The reaction condition were 500 ppm NH_3, 500 ppm NO, 150 °C and a GHSV = 478000 h^{-1}. NH_3 decreased the Hg^0 capacity of $LaMnO_3$, and the Hg^0 capacities decreased to 5.88 mg/g compared to 6.22 mg/g only under only 4% O_2. However, NO enhanced the Hg^0 adsorption capacity, and the Hg^0 capacity was 7.18 mg/g after 600 min of adsorption. When the gas component was 4% O_2 + 500 ppm NO + 500 ppm NH_3, the Hg^0 capacity decreased compared to that with 4% O_2 + 500 ppm NO and increased compared to that with 4% O_2 + 500 ppm NH_3.

To investigate the NH_3 surface oxidation and NO oxidation performance, $NH_3 + O_2$-TPD and $NO + O_2$-TPD was performed in our study. A FT–IR gas analyzer was employed to detect the gas component along with the increase of temperature. As shown in Fig. 10(a), when the temperature increased from 50 °C, the adsorbed NH_3 started to release from the surface of $LaMnO_3$, and this NH_3 was due to the physical-adsorbed NH_3 (ad-NH_3) on the $LaMnO_3$ surface. At a temperature of 150 °C, N_2O was detected. As the temperature increased to 400 °C, NO was released from the $LaMnO_3$ surface. The ad-NH_3 may be oxidized to N_2O at low temperatures and NO at higher temperatures. The $NO + O_2$-TPD was also investigated in this study. As shown in Fig. 10(b), the adsorbed-NO (ad-NO) started to desorb from the surface of $LaMnO_3$ at 150 °C. As the temperature increased to 200 °C, NO_2 started to release. The ad-NO was most likely oxidized to NO_2 by catalytic oxidation over $LaMnO_3$. The mechanism of NH_3-SCR reaction over $LaMnO_3$ has been previously reported, especially for the reaction following the L-H mechanism [32,34]. It is unnecessary to distinguish the species on the $LaMnO_3$ surface after NH_3/NO adsorption in previous studies based on DRIFTs studies. The desorbed NH_3 can be assigned as ad-NH_3, and the desorbed NO can be assigned to NH_3 bond to acid sites [34]. Therefore, ad-NH_3 formed NH_4^+ on the surface covered the active sites and consumed surface oxygen, which inhibited Hg^0 oxidation, resulting in a low removal efficiency. However, the ad-NO formed NO_2 on the surface of $LaMnO_3$, and these species are most likely responsible for Hg^0 oxidation [38].

3.2.5. Effect of SO_2 and H_2 on Hg^0 removal

The effects of SO_2 and H_2O on Hg^0 removal were also investigated (Fig. 11). SO_2 had an adverse effect on the Hg^0 removal, and Hg^0 capacity decreased approximately 20% when 500 ppm SO_2 was included in the simulated gas. SO_2 may easily react with Mn-based materials to form Mn–SO_4^{2-} [38,39]. NH_3 resulted in a decrease in the Hg^0 capacity when SO_2 was present, but NO promoted Hg^0 removal even when SO_2 was included in the simulated gas. NH_3 can react with SO_2 to form sulfate species, and causes catalyst deactivation. However, the existence of H_2O had an adverse effect on Hg^0 adsorption, especially when NH_3 and NO co-existed. Therefore, NO may form nitrate which results in a loss in oxidation performance. Furthermore, the active sites of $LaMnO_3$ were occupied, resulting in low adsorption capacities. Moreover, the presence of both SO_2 and H_2O had a serious adverse effect on Hg^0 removal over $LaMnO_3$, and the Hg^0 capacity was only 50% compare to that under N_2 + 4%O_2. When NH_3 and NO were added to the simulated gas, the Hg^0 adsorption capacity further decreased, and the capacity decreased to only 2.5 mg/g under 4% O_2 + 4% H_2O + 500 ppm NH_3 + 500 ppm NO + 500 ppm SO_2. It is interesting to further discuss the mechanism for the interaction among the H_2O, NH_3 and NO (Fig. 11).

3.3. Mercury temperature-programmed-desorption (Hg-TPD)

The mercury temperature-programmed-desorption (Hg-TPD) method was performed. In addition, the desorption activation energy (E_d) was calculated to explain the binding force between mercury and $LaMnO_3$. The adsorption under different gas atmo-

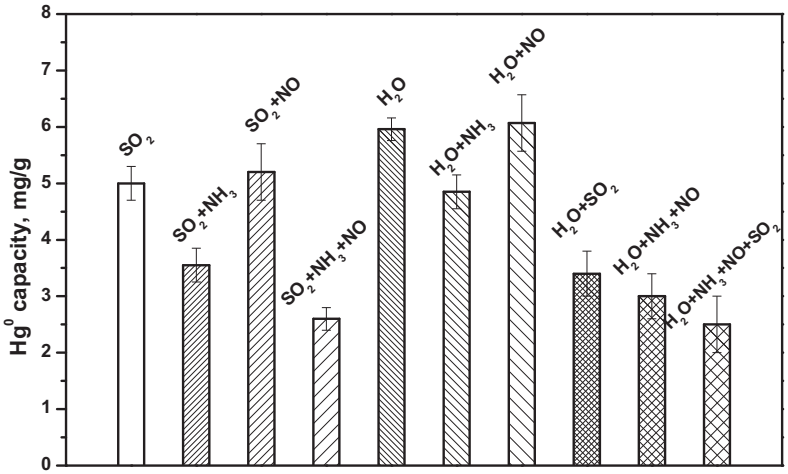

Fig. 11. Effects of SO_2 and H_2O on the Hg^0 adsorption capacity. Reaction condition: 150 °C; GHSV = 478,000 h^{-1}; O_2: 4%; NH_3: 500 ppm; NO: 500 ppm; SO_2: 500 ppm; H_2O: 4%.

sphere and desorption under pure N_2 was first studied. The Hg-TPD model for the E_d calculation was as follows:

The Hg^0 desorption process was assumed as to follow first-order kinetics [40–42]:

$$\frac{r_d}{N_s} = -\frac{d\theta}{dt} = k_d\theta \quad (7)$$

where r_d is the desorption rate of mercury from the sorbent (mol/min), N_s is the maximum mercury concentration on the unit surface of the sorbent (mol/cm^2), θ is the transient coverage of mercury, t is the time (min) and k_d is the desorption rate.

Based on Eq. (7), the related parameters can be defined as follows:

$$k_d = A\exp\left(-\frac{E_d}{RT}\right) \quad (8)$$

$$\frac{r_d}{N_s} = -\frac{d\theta}{dt} = A\theta\exp\left(-\frac{E_d}{RT}\right) \quad (9)$$

$$T = T_0 + \beta t \quad (10)$$

where R is the gas constant, T is the temperature, A is the pre-exponential factor, β (K/min) is the heating rate and T_0 (K) is the initial temperature of TPD experiment. Assuming that the desorption rate reaches a maximum value at a certain temperature T_p (K), then $dr_d/dt = 0$, and Eq. (7) can be expressed as follows:

$$2\ln T - \ln\beta = \frac{E_d}{RT_p} + \ln\frac{E_d}{AR} \quad (11)$$

Based on Eq. (11), the Hg-TPD curves under different heating rates are created by plotting of $\left(2\ln T_p - \ln\beta\right)$ as a function of $1/T_p$, which generates a linear relationship, and E_d can be calculated.

First, the Hg-TPD experiments were performed using different gas components. N_2 + Hg-TPD, O_2 + Hg-TPD, $NH_3 + O_2$ + Hg-TPD, $NO + O_2$ + Hg-TPD and $SO_2 + O_2$ + Hg-TPD were tested. As shown in Fig. 12, the adsorption under pure N_2 resulted in two peaks. One peak located at approximately 248.5 °C was due to physical-adsorption on the $LaMnO_3$ surface. The primary desorption peak at approximately 342.5 °C may be associated with chemical-adsorption. For adsorption under 4% O_2, the desorption peak was located at 361.5 °C which is higher than the second peak under N_2. Based on Equation (8), as the desorption temperature increased, the desorption energy increased. For adsorption under $NH_3 + O_2$ and $NO + O_2$, the primary desorption peaks were centered at 345.5 and 356.5 °C, respectively. The desorption peaks under O_2, $NH_3 + O_2$ and $NO + O_2$ adsorption atmosphere were similar. However, for adsorption under $SO_2 + O_2$, desorption began at approximately 230 °C,

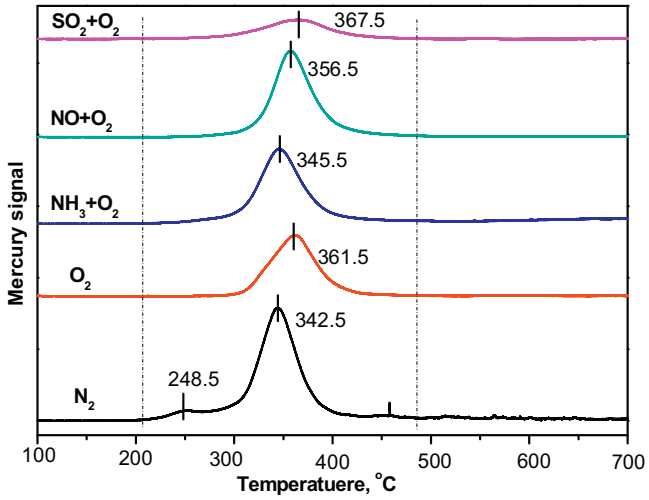

Fig. 12. Hg-TPD curves for $LaMnO_3$ under different adsorption conditions.

which is lower than that of under an O_2 atmosphere. In addition, a wide peak was observed in the curve of under $SO_2 + O_2$. The sulfate (SO_4^{2-}) on $LaMnO_3$ surface may have affected the Hg-O binding energy. The desorption energy based on Eq. (8) was calculated, and the O_2 + Hg-TPD for a desorption rate of 2, 5 and 10 °C/min is shown in Fig. S3. The desorption activation energy was 150.50 kJ/mol. $LaMnO_3$ can be regenerated by thermal desorption. The sample was re-used for Hg^0 adsorption, as shown in Fig. S4, and the Hg^0 capacities were nearly the same after the 5th adsorption run. The results indicated that $LaMnO_3$ can be fully regenerated.

Based on these results, the optimal reaction temperature for NO conversion is 200–250 °C and Hg^0 adsorption is 100–150 °C. In coal-fired power plants, the catalyst can be used downstream of ESP/FF, and in this section, the temperature is approximately 200 °C. A low-temperature NH_3-SCR catalyst was also used in this section. $LaMnO_3$ had a NO removal efficiency of approximately 60–70% and a higher Hg^0 capacity. In a traditional coal-fired power plant, the NO concentration decreases after the SCR reaction, and the Hg^0 concentration also decreased after the SCR catalyst and ESP/FF. Therefore, the low-temperature NH_3-SCR reactor may also be beneficial for simultaneous removal of Hg^0 and NO.

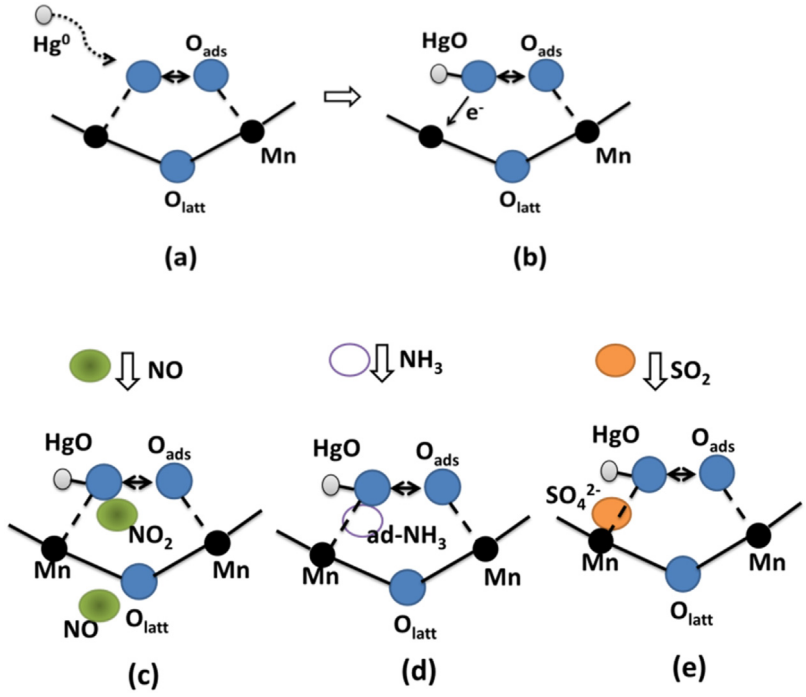

Fig. 13. Proposed reaction mechanism for Hg^0 adsorption under different gas compositions over $LaMnO_3$.

4. Conclusions

In this study, $LaMnO_3$ perovskite oxide, which was used as a low-temperature NH_3-SCR catalyst, was confirmed to be a Hg^0 sorbent. The perovskite structure was beneficial for Hg^0 catalytic oxidation and adsorption, and the reduction of Mn^{4+} to Mn^{3+} results in oxidation of Hg^0 to Hg^{2+}. The adsorbed oxygen combined with Hg^{2+} to form HgO species on the $LaMnO_3$ surface. The adsorption mechanism is briefly illustrated in Fig. 13, the Hg^0 first adsorbed on $LaMnO_3$ surface, then Hg^0 was oxidized to Hg^{2+} and existed as HgO species. In addition, the existence of NO enhanced the Hg^0 capacity but the presence of NH_3 inhibited Hg^0 adsorption. NO adsorption on $LaMnO_3$ may result in the formation of NO_2, which is favorable for Hg^0 oxidation. However, the existence of ad-NH_3 occupied the adsorbed oxygen, resulting in difficulties with Hg–O bonding. The existence of SO_2 also decreased the Hg^0 capacity due to the sulfate generated on the $LaMnO_3$ surface. A further improvement in the $LaMnO_3$ materials is currently underway. $LaMnO_3$ exhibited superior performance for Hg^0 adsorption and is an ideal material for the simultaneous removal of Hg^0 and NO at low-temperatures in coal-fired power plants.

Acknowledgement

This study was supported by the Major State Basic Research Development Program of China (973 Program, No. 2013CB430005), the National Natural Science Foundation of China (No. 51478261 and No. 51278294). Thanks for Shanghai Tongji Gao Tingyao Environmental Science and Technology Development Foundation.

Appendix A. Supplementary data

Supplementary data associated with this article can be found, in the online version, at http://dx.doi.org/10.1016/j.apcatb.2015.12.042.

References

[1] W.H. Schroeder, J. Munthe, Atmos. Environ. 32 (1998) 809–822.
[2] N. Pirrone, P. Costa, J. Pacyna, R. Ferrara, Atmos. Environ. 35 (2001) 2997–3006.
[3] K.-H. Kim, V.K. Mishra, S. Hong, Atmos. Environ. 40 (2006) 3281–3293.
[4] Z.-W. Wang, Z.-S. Chen, D. Ning, X.-S. Zhang, J. Environ. Sci. 19 (2007) 176–180.
[5] D.G. Streets, J. Hao, Y. Wu, J. Jiang, M. Chan, H. Tian, X. Feng, Atmos. Environ. 39 (2005) 7789–7806.
[6] H. Kamata, S.-I. Ueno, T. Naito, A. Yukimura, Ind. Eng. Chem. Res. 47 (2008) 8136–8141.
[7] M. Dĺaz-Somoano, S. Unterberger, K.R. Hein, Fuel Proc. Technol. 88 (2007) 259–263.
[8] Y. Eom, S.H. Jeon, T.A. Ngo, J. Kim, T.G. Lee, Catal. Lett. 121 (2008) 219–225.
[9] R.D. Vidic, D.P. Siler, Carbon 39 (2001) 3–14.
[10] W. Liu, R.D. Vidic, T.D. Brown, Environ. Sci. Technol. 34 (2000) 483–488.
[11] J. Wo, M. Zhang, X. Cheng, X. Zhong, J. Xu, X. Xu, J. Hazard. Mater. 172 (2009) 1106–1110.
[12] S.J. Lee, Y.-C. Seo, J. Jurng, T.G. Lee, Atmos. Environ. 38 (2004) 4887–4893.
[13] Z. Shen, J. Ma, Z. Mei, J. Zhang, J. Environ. Sci. 22 (2010) 1814–1819.
[14] M.H. Kim, S.-W. Ham, J.-B. Lee, Appl. Catal. B: Environ. 99 (2010) 272–278.
[15] Y. Li, P.D. Murphy, C.-Y. Wu, K.W. Powers, J.-C.J. Bonzongo, Environ. Sci. Technol. 42 (2008) 5304–5309.
[16] B. Thirupathi, P.G. Smirniotis, J. Catal. 288 (2012) 74–83.
[17] Y.J. Kim, H.J. Kwon, I. Heo, I.-S. Nam, B.K. Cho, J.W. Choung, M.-S. Cha, G.K. Yeo, Appl. Catal. B: Environ. 126 (2012) 9–21.
[18] J. Li, H. Chang, L. Ma, J. Hao, R.T. Yang, Catal. Today 175 (2011) 147–156.
[19] S. Straube, T. Hahn, H. Koeser, Appl. Catal. B: Environ. 79 (2008) 286–295.
[20] Y. Gao, Z. Zhang, J. Wu, L. Duan, A. Umar, L. Sun, Z. Guo, Q. Wang, Environ. Sci. Technol. 47 (2013) 10813–10823.
[21] Y. Nishihata, J. Mizuki, T. Akao, H. Tanaka, M. Uenishi, M. Kimura, T. Okamoto, N. Hamada, Nature 418 (2002) 164–167.
[22] J. Suntivich, K.J. May, H.A. Gasteiger, J.B. Goodenough, Y. Shao-Horn, Science 334 (2011) 1383–1385.
[23] Y. Teraoka, K. Kanada, S. Kagawa, Appl. Catal. B-Environ. 34 (2001) 73–78.
[24] R. Spinicci, A. Tofanari, M. Faticanti, I. Pettiti, P. Porta, J. Mol. Catal. A-Chem. 176 (2001) 247–252.
[25] C. Tofan, D. Klvana, J. Kirchnerova, Appl. Catal. B-Environ. 36 (2002) 311–323.
[26] B. Tang, J. Ge, C. Wu, L. Zhuo, J. Niu, Z. Chen, Z. Shi, Y. Dong, Nanotechnology 15 (2004) 1273.
[27] J. Chen, M. Shen, X. Wang, G. Qi, J. Wang, W. Li, Appl. Catal. B: Environ. 134–135 (2013) 251–257.
[28] J. Li, N. Yan, Z. Qu, S. Qiao, S. Yang, Y. Guo, P. Liu, J. Jia, Environ. Sci. Technol. 44 (2009) 426–431.
[29] C. He, B. Shen, J. Chen, J. Cai, Environ. Sci. Technol. 48 (2014) 7891–7898.
[30] N. Russo, D. Fino, G. Saracco, V. Specchia, J. Catal. 229 (2005) 459–469.
[31] H. Xu, Z. Qu, C. Zong, W. Huang, F. Quan, N. Yan, Environ. Sci. Technol. (2015).
[32] R. Zhang, N. Luo, W. Yang, N. Liu, B. Chen, J. Mol. Catal. A: Chem. 371 (2013) 86–93.
[33] H. Li, C.-Y. Wu, Y. Li, J. Zhang, Appl. Catal. B: Environ. 111 (2012) 381–388.

[34] R. Zhang, W. Yang, N. Luo, P. Li, Z. Lei, B. Chen, Appl. Catal. B: Environ. 146 (2014) 94–104.
[35] H. Xu, J. Xie, Y. Ma, Z. Qu, S. Zhao, W. Chen, W. Huang, N. Yan, Fuel 140 (2015) 803–809.
[36] H. Xu, Z. Qu, S. Zhao, J. Mei, F. Quan, N. Yan, J. Hazard. Mater. 299 (2015) 86–93.
[37] J. Xie, H. Xu, Z. Qu, W. Huang, W. Chen, Y. Ma, S. Zhao, P. Liu, N. Yan, J. Colloid Interface Sci. 428 (2014) 121–127.
[38] H. Li, C.-Y. Wu, Y. Li, L. Li, Y. Zhao, J. Zhang, J. Hazard. Mater. 243 (2012) 117–123.
[39] S. Yang, Y. Guo, N. Yan, D. Wu, H. He, J. Xie, Z. Qu, J. Jia, Appl. Catal. B: Environ. 101 (2011) 698–708.
[40] H.X. Xi, Z. Li, H.B. Zhang, X. Li, X.J. Hu, Sep. Purif. Technol. 31 (2003) 41–45.
[41] Z. Li, H.J. Wang, H.X. Xi, Q.B. Xia, J.L. Han, L.A. Lu, Adsorpt. Sci. Technol. 21 (2003) 125–133.
[42] R.T. Yang, R.Q. Long, J. Padin, A. Takahashi, T. Takahashi, Ind. Eng. Chem. Res. 38 (1999) 2726–2731.